

Revisiting Stochastic Gravitational Wave Background in the Strong Signal Case

Zheng-Cheng Liang,¹ Zhi-Yuan Li,¹ En-Kun Li,¹ Jian-dong Zhang,¹ and Yi-Ming Hu^{1,*}

¹*MOE Key Laboratory of TianQin Mission, TianQin Research Center for Gravitational Physics
& School of Physics and Astronomy, Frontiers Science Center for TianQin, CNSA Research
Center for Gravitational Waves, Sun Yat-sen University (Zhuhai Campus), Zhuhai 519082, China*

(Dated: August 22, 2024)

Weak-signal limit is often used in estimating stochastic gravitational-wave background (SGWB) intensities. This approximation fails and the signal-to-noise ratio (SNR) can be much weaker when background signals are loud compared to the detector noise. In this work, we find that this issue is especially significant when dealing with networks of detectors that are widely separated. For the TianQin + LISA network, the SNR estimated under the weak-signal limit might be off by as large as an order of magnitude. Contour plots of SNR over the parameter spaces are also presented to indicate regions that will be affected by this correction. Our results suggest that DA and DB type extragalactic double white dwarfs may yield an SGWB with SNR surpassing 100 after 1 year of operation in weak-signal limit scenario, with a redshift-independent merger rate of about $500 \text{ Mpc}^{-3} \text{ Myr}^{-1}$. In fact, this value falls significantly below the necessary threshold. Similar influences arise for first-order phase transitions, yet pinning down the detectable parameters remains formidable due to model uncertainties.

I. INTRODUCTION

The stochastic gravitational-wave (GW) background (SGWB) is a superposition of independent and unresolvable GW from diverse sources, with the astrophysical component including binary black hole (BBH), binary neutron star (BNS), double white dwarf (DWD), etc [1, 2]. Alternatively, the cosmological component traces back to early Universe processes, such as inflation, first-order phase transitions (PTs), and cosmic defects [3, 4]. This diversity enables the SGWB to cover multiple frequency ranges. A recent significant milestone was made by collaborations utilizing Pulsar Timing Arrays (PTA), offering compelling evidence for the existence of SGWB in the nanoHertz (nHz) band [5–8]. While ground-based GW detectors have yet to detect the SGWB in the hundred-hertz frequency band, the upper limit of SGWB intensity in this range has been estimated based on available observation data [9]. In the future, with the potential advancements in space-borne GW detectors, SGWB could be detected within the millihertz (mHz) frequency band [10, 11].

Space-borne GW detectors, like TianQin [10], Laser Interferometer Space Antenna (LISA) [11], are typically composed of three satellites arranged in an equilateral triangle formation. However, the unequal armlengths resulting from detector motion present a challenge in canceling laser noise, leading to the requirement of time delay interferometry (TDI) technique [12, 13]. Among the various TDI combinations, the unequal-arm Michelson with the noise-orthogonal basis (A,E,T) is commonly employed. The A/E channels are specifically tailored for detecting GW, providing optimized detection sensitivity [14]. The T channel exhibits a substantially lower

sensitivity to GW compared to the A/E channels, making it more suitable for monitoring detector noise rather than efficiently detecting GW [15].

One often relies on the auto- or cross-correlation of the channel data to derive the power spectral density (PSD) of SGWB. The null-channel method utilizes the auto-correlation of the null channel to effectively track and isolate noises, allowing for the identification of the SGWB component within a single space-borne detector [15–21]. While in scenarios where a network of space-borne detectors is deployed, each responding to a common SGWB but with uncorrelated noises, distinguishing between the SGWB and detector noise can be achieved through cross-correlating the channel data from two or more detectors [22–29].

Following the null-channel and cross-correlation methods, the expectation of detection measurement is primarily determined by the PSD of SGWB and the overlap reduction function (ORF), which quantifies the reduction in the correlation to an SGWB resulting from the relative separation and orientation of the channels. On the other hand, the variance of detection measurement is solely influenced by the noise PSD, given the SGWB is significantly lower than the detector noise (weak-signal limit). Based on the expectation and variance, the detection signal-to-noise ratio (SNR) can be calculated, taking into account factors such as correlation time accumulation and frequency band integration. Building upon the SNR for the weak-signal limit, the power-law integrated sensitivity (PLIS) and peak-integrated sensitivity (PIS) sensitivity curve is derived and commonly used to showcase the detection capability for the SGWB [30, 31]. Additionally, inversely solving the SNR can be employed to constrain the detectable regions of source parameters, as exemplified by SNR contour plots [32–34].

While the weak-signal limit is applicable in most scenarios, there may exist SGWB with intensities matching or exceeding the detector noise [35–43]. Therefore,

* huyiming@sysu.edu.cn

Allen et al. extended the SNR to handle arbitrarily large SGWB, specifically tailored for an ORF-invariant channel pair [26, 44, 45]. They highlighted that the existence of SGWBs can impact the variance of detection measurements, potentially resulting in an overestimation of detection capability [26, 44, 45]. This SNR estimator has been applied in a series of subsequent studies [29, 46–48]. However, to the best of our knowledge, it has not been utilized for constructing PLIS and PIS sensitivity curves, nor in generating SNR contour plots.

In this paper, we further develop a more robust SNR estimation, adaptable to multiple channel pairs and time-varying ORF. By incorporating the correction of the SNR estimation, we revise the PLIS and PIS sensitivity curves. Focusing on TianQin, the TianQin I+II network, and the TianQin + LISA network, we identify gaps in sensitivity curves between the scenarios of approximation and non-approximation. Additionally, to illustrate the gaps in constraining detectable parameter regions between these two scenarios, we employ the SNR contour plot.

The structure of the paper is as follows. In Sec. II, we introduce the space mission discussed in this study. Sec. III and IV are dedicated to SGWB detection with and without the weak-signal limit. The case study is presented in Sec. V. Finally, a brief conclusion and discussion is provided in Sec. VI.

II. SPACE MISSION

Several space missions have been proposed for GW detection, such as TianQin [10], LISA [11], among others. This paper specifically centers on the TianQin and LISA missions.

A. detector design

As shown in Fig. 1, TianQin is a space-borne GW detector comprising three identical satellites in Earth’s orbit. These satellites will have a 3.64-day orbital period and will be positioned at a radius of approximately 10^5 km. When operational, they will form an equilateral triangle with an arm length (L_{TQ}) of about 1.7×10^5 km. TianQin will operate on a “three months on + three months off” schedule, with a proposed second mission, TianQin II, aimed at filling detection gaps [49]. The orbital planes of TianQin and TianQin II are arranged perpendicular to each other, creating the TianQin I+II network. The nominal work scheme leads to no overlap in the operation times of TianQin and TianQin II; we instead consider a scenario where the observation time can be extended and correspond to an enhanced operational mode of “four months on + two months off”.

LISA, on the other hand, is designed to orbit the Sun, trailing Earth by approximately 20° and maintaining a

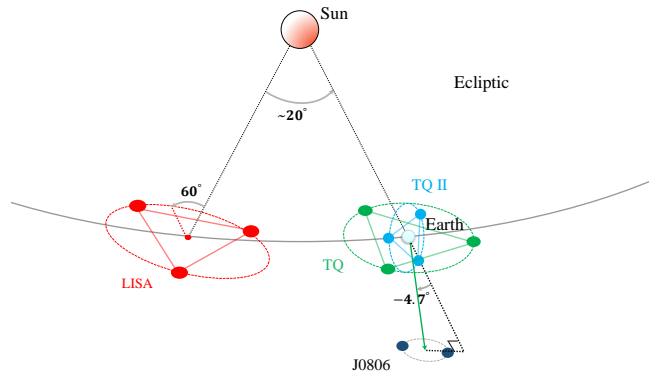


FIG. 1. Schematic diagram of TianQin, TianQin II, and LISA in the ecliptic plane.

fixed 60° angle with the ecliptic plane. It will comprise three satellites separated by a distance of about 2×10^6 km, forming the armlength (L_{LISA}) of the detector. LISA will share the similar operating period and detection band as TianQin, which opens up the opportunity to establish the TianQin + LISA network, allowing for a half-a-year overlap within 1 year.

For convenience, shorthand notations can be used in figures and equations: TQ for TianQin, TQ II for TianQin II, TT for the TianQin I+II network, and TL for the TianQin + LISA network.

B. TDI channel

Due to the detector motion, maintaining an equilateral shape for a space-borne detector is challenging, making it difficult to implement an equal-arm Michelson to cancel laser noise. In response to this challenge, the TDI combination has been proposed [12]. The first-generation TDI is initially designed for static detectors and includes components such as the Sagnac, unequal-arm Michelson, Relay, Monitor, and Beacon [13]. This paper focuses on the unequal-arm Michelson (X,Y,Z), which can be established using each satellite and its adjacent link. Furthermore, the corresponding noise-orthogonal bases can be constructed by [14]

$$\begin{aligned} A &= \frac{1}{\sqrt{2}}(Z - X), \\ E &= \frac{1}{\sqrt{6}}(X - 2Y + Z), \\ T &= \frac{1}{\sqrt{3}}(X + Y + Z). \end{aligned} \quad (1)$$

Following the successful cancel of laser noise, secondary noise, including optical-path noise and acceleration noise, become more pronounced. Assuming stationary noise conditions, the PSD for the TDI channel (A, E, T) can be calculated by

$$\begin{aligned}
P_{\text{nA/E}}(f) &= \frac{2 \sin^2 \left[\frac{f}{f_*} \right]}{L^2} \left[\left(\cos \left[\frac{f}{f_*} \right] + 2 \right) S_p(f) + 2 \left(\cos \left[\frac{2f}{f_*} \right] + 2 \cos \left[\frac{f}{f_*} \right] + 3 \right) \frac{S_a(f)}{(2\pi f)^4} \right], \\
P_{\text{nT}}(f) &= \frac{8 \sin^2 \left[\frac{f}{f_*} \right] \sin^2 \left[\frac{f}{2f_*} \right]}{L^2} \left(S_p(f) + 4 \sin^2 \left[\frac{f}{2f_*} \right] \frac{S_a(f)}{(2\pi f)^4} \right),
\end{aligned} \tag{2}$$

where the characteristic frequency $f_* = c/(2\pi L)$, S_p and S_a represent the PSDs of optical-path noise and acceleration noise, respectively. For more comprehensive information on the parameters of TianQin and LISA, readers are encouraged to refer to Refs. [50, 51]. Unless otherwise stated, our study primarily focuses on the case with using the A/E/T channels.

III. FORMALISM

A. Stochastic background

In the transverse-traceless gauge, the metric perturbation of an SGWB can be expressed as a superposition of plane wave:

$$\begin{aligned}
h(t, \vec{x}) &= \sum_{P=+, \times} \int_{-\infty}^{\infty} df \int_{S^2} d\hat{\Omega}_{\hat{k}} \tilde{h}_P(f, \hat{k}) \mathbf{e}^P(\hat{k}) \\
&\quad \times e^{i2\pi f[t - \hat{k} \cdot \vec{x}(t)/c]},
\end{aligned} \tag{3}$$

where the wave vector of the gravitational wave is denoted by \hat{k} , the polarization tensor $\mathbf{e}^P(\hat{k})$ refers to the polarization P of the GW, the speed of light is represented by c .

To begin, we narrow our focus to the Gaussian-stationary, unpolarized, and isotropic SGWB. Therefore, it is reasonable to assume that the SGWB possesses a zero-mean Fourier amplitude $\tilde{h}_P(f, \hat{k})$, with the direction-dependent PSD \mathcal{P}_h :

$$\langle \tilde{h}_P(f, \hat{k}) \tilde{h}_{P'}^*(f', \hat{k}') \rangle = \frac{1}{4} \delta(f - f') \delta_{PP'} \delta^2(\hat{k} - \hat{k}') \mathcal{P}_h(|f|, \hat{k}). \tag{4}$$

Here the factor $1/4$ stems from both the definition of one-side PSD and the average of polarization, δ_{ij} denotes the Kronecker delta. The PSD of SGWB incorporates contributions from all directions in the sky, as reflected in the all-sky integral of the \mathcal{P}_h :

$$\begin{aligned}
S_h(f) &= \int_{S^2} d\hat{\Omega}_{\hat{k}} \mathcal{P}_h(f, \hat{k}) \\
&= 4\pi \mathcal{P}_h(f)
\end{aligned} \tag{5}$$

where the second line of this equation is derived under the assumption of isotropy in the SGWB.

To further characterize the distribution of energy across different frequencies in the SGWB, a commonly used quantity is the dimensionless energy spectrum density Ω_{gw} . This quantity serves to capture the ratio of GW

energy density $d\rho_{\text{gw}}$ within a specific frequency range $[f, f + df]$ to the critical energy density ρ_c , exhibiting a direct relationship with S_h [30, 52]:

$$\Omega_{\text{gw}}(f) = \frac{1}{\rho_c} \frac{d\rho_{\text{gw}}}{d(\ln f)} = \frac{2\pi^2}{3H_0^2} f^3 S_h(f), \tag{6}$$

where the critical energy density is defined as $\rho_c = 3H_0^2 c^2 / (8\pi G)$, with the gravitational constant G , and the Hubble constant H_0 .

B. Overlap reduction function

The SGWB signal $h_I(t)$, observed in detector channel I , can be expressed as the convolution of the metric perturbations $h(t, \vec{x})$ and the detector response $\mathbb{D}^{ab}(t, \vec{x})$ [53]. To simplify the measurement process without compromising accuracy, one can focus on a narrow time scale, namely $[t_0 - T/2, t_0 + T/2]$, during which the assumption can be made that the channel response remains unchanged. By employing the short-term Fourier transform within this time interval, we have:

$$\begin{aligned}
h_I(t, t_0) &= \mathbb{D}_I[t, \vec{x}(t_0)] * h[t, \vec{x}(t_0)] \\
&= \sum_{P=+, \times} \int_{-\infty}^{\infty} df \int_{S^2} d\hat{\Omega}_{\hat{k}} F_I^P(f, \hat{k}, t_0) \tilde{h}_P(f, \hat{k}) \\
&\quad \times e^{i2\pi f[t - \hat{k} \cdot \vec{x}(t_0)/c]},
\end{aligned} \tag{7}$$

where the position vector of the measurement at time t is denoted by \vec{x} , the channel response is represented as the double contraction of the channel tensor and the polarization tensor [54].

In terms of the frequency domain SGWB signal

$$\begin{aligned}
\tilde{h}_I(f, t_0) &= \sum_{P=+, \times} \int_{S^2} d\hat{\Omega}_{\hat{k}} F_I^P(f, \hat{k}, t_0) \tilde{h}_P(f, \hat{k}) \\
&\quad \times e^{-i2\pi f \hat{k} \cdot \vec{x}(t_0)/c},
\end{aligned} \tag{8}$$

the PSD of SGWB signals is determined by

$$\langle \tilde{h}_I(f, t_0) \tilde{h}_J^*(f', t_0) \rangle = \frac{1}{2} \delta(f - f') \Gamma_{IJ}(f, t_0) S_h(|f|). \tag{9}$$

Here, $I = J$ corresponds to the auto PSD of one channel, while $I \neq J$ indicates the cross PSD of two channels. Combined with Eq. (4), Eq. (5), Eq. (8), and Eq. (9), the ORF

$$\Gamma_{IJ}(f, t_0) = \frac{1}{4\pi} \int_{S^2} d\hat{\Omega}_{\hat{k}} \mathcal{Y}_{IJ}(f, \hat{k}, t_0), \tag{10}$$

where the antenna pattern involves both the channel response and the separation vector $\Delta\vec{x} = \vec{x}_I - \vec{x}_J$ between detectors:

$$\mathcal{Y}_{IJ}(f, \hat{k}, t_0) = \frac{1}{2} \sum_{P=+, \times} F_I^P(f, \hat{k}, t_0) F_J^{P*}(f, \hat{k}, t_0) \times e^{-i2\pi f \hat{k} \cdot [\vec{x}_I(t_0) - \vec{x}_J(t_0)]/c}, \quad (11)$$

Note that, for triangular-shaped detectors, it is convenient to designate one of the vertices as the reference point for the detector position, facilitating the determination of the separation vector between two detectors [48].

$$S_{IJ} = \int_{t_0-T/2}^{t_0+T/2} dt \int_{t_0-T/2}^{t_0+T/2} dt' [s_I(t) s_J(t') - \langle n_I(t) n_J(t') \rangle] Q_{IJ}(t, t'), \quad (13)$$

where

$$\langle n_I(t) n_J(t') \rangle = \frac{1}{2} \int_{-\infty}^{\infty} df e^{-i2\pi f(t-t')} P_{n_{IJ}}(|f|). \quad (14)$$

For uncorrelated channels, $\langle n_I(t) n_J(t') \rangle = 0$, so Eq. (13) reduces to Eq. (12). In real data analysis, the noise PSD needs to be determined through the observation data, which inevitably contains random fluctuation. Fortunately, by utilizing the smooth and stationary property of the noise PSD, we can greatly reduce its random fluctuation by adopting the averaged periodogram method [55–57].

Integrating Eq. (12) into Eq. (13) is a straightforward process that unifies the measurements obtained by the cross-correlation and null-channel methods. In the subsequent analysis, we will examine the SGWB detection using the unified measurement S_{IJ} for both methods. To further streamline subsequent analysis, we designate the detectors as \mathcal{A} and \mathcal{B} . Assuming that the employed channels in each detector share the same auto-correlation ORF $\mathcal{R}_{\mathcal{A}}$ and noise PSD, the total SNR in the weak-signal limit [58, 59]

$$\rho_{\text{tot}} = \left[\frac{2 T_{\text{tot}}}{1 + \delta_{\mathcal{AB}}} \int_{f_{\min}}^{f_{\max}} df \frac{\bar{\Gamma}_{\text{tot}}^2(f) \Omega_{\text{gw}}^2(f)}{\hat{D}_{\mathcal{AB}}(f)} \right]^{1/2}, \quad (15)$$

where T_{tot} and $[f_{\min}, f_{\max}]$ denote the total correlation time and the detection band, respectively. The total time-averaged ORF

$$\bar{\Gamma}_{\text{tot}}(f) = \sqrt{\frac{1}{T_{\text{tot}}} \int_0^{T_{\text{tot}}} dt_0 \sum_{IJ} |\Gamma_{IJ}(f, t_0)|^2}. \quad (16)$$

C. Detection sensitivity

The data s_I is the linear addition of the SGWB signal h_I and the noise n_I . For channels I and J from two independent detectors, we can define their cross-correlation as [26]:

$$S'_{IJ} = \int_{t_0-T/2}^{t_0+T/2} dt \int_{t_0-T/2}^{t_0+T/2} dt' s_I(t) s_J(t') Q_{IJ}(t, t'), \quad (12)$$

where Q_{IJ} is a filter function that can be determined in the aim to maximize the SNR of the SGWB. Notice though, for reasons that we will explain in detail later, when the noises from channels I and J have non-zero correlation, then the above definition of channel correlation needs to be extended as [18]:

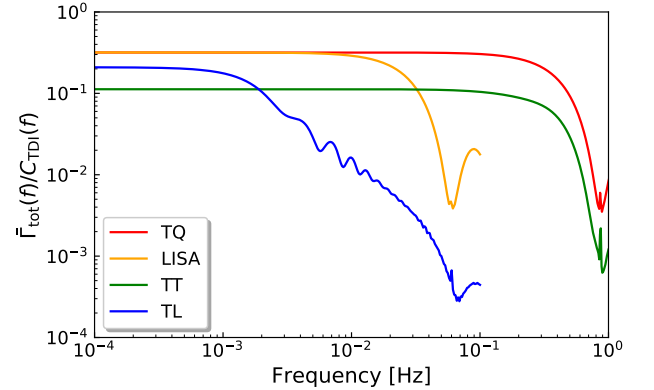


FIG. 2. Normalized ORF for TianQin (red), LISA (orange), the TianQin I+II network (green), and the TianQin + LISA network (blue).

The denominator of the integral term

$$\hat{D}_{\mathcal{AB}}(f) = \mathcal{R}_{\mathcal{A}}(f) \mathcal{R}_{\mathcal{B}}(f) \Omega_{n_{\mathcal{A}}}(f) \Omega_{n_{\mathcal{B}}}(f), \quad (17)$$

with the noise energy spectrum density

$$\Omega_{n_{\mathcal{A}}}(f) = \frac{2\pi^2}{3H_0^2} f^3 \frac{P_{n_{\mathcal{A}}}(f)}{\mathcal{R}_{\mathcal{A}}(f)}. \quad (18)$$

Figure 2 presents the ORF for TianQin, LISA, the TianQin I+II network, and the TianQin + LISA network, employing the A/E channels. To account for the frequency-dependent factor introduced by the TDI, the ORF is normalized by $C_{\text{TDI}}(f) = 4 \sin[2\pi f L/c] \sin[2\pi f L'/c]$, where $L = L'$ for a single

detector [44, 60]. It is observed that the total ORF for cross-correlation between two detectors is much lower than that for the auto-correlation of each respective detector channel within the mHz frequency band. This effect becomes notably pronounced for the TianQin + LISA network, where the large separation results in a considerable decrease in the drop frequency of ORF. Furthermore, it is worth mentioning that for the A/E channels of the same detector, the cross-correlation ORF is equal to 0.

The next step involves the analysis of the sensitivity curve. Considering an SGWB characterized by the energy density spectrum that follows a power-law distribution:

$$\Omega_{\text{gw}}(f) = \Omega_0(\epsilon)(f/f_{\text{ref}})^\epsilon|_{\epsilon=\epsilon_0}, \quad (19)$$

the SNR threshold ρ_{thr} , beyond which the GW detectors can find the SGWB, can be translated into the threshold of SGWB strength Ω_0 based on Eq. (15):

$$\Omega_0(\epsilon) = \rho_{\text{thr}} \left[\frac{2T_{\text{tot}}}{1 + \delta_{\text{AB}}} \int_{f_{\text{min}}}^{f_{\text{max}}} df \frac{\bar{\Gamma}_{\text{tot}}^2(f)(f/f_{\text{ref}})^{2\epsilon}}{\hat{D}_{\text{AB}}(f)} \right]^{-1/2}, \quad (20)$$

where the reference frequency f_{ref} is arbitrary. Subsequently, by considering each frequency with a specific index ϵ , the PLIS curve can be generated by

$$\Omega_{\text{PLIS}}(f) = \max_{\epsilon} [\Omega_0(\epsilon)(f/f_{\text{ref}})^\epsilon]. \quad (21)$$

This sensitivity curve, typically plotted on a logarithmic scale, characterizes the collective envelopes of power-law SGWBs where the SNR aligns with the preset threshold. Detection expectations for an SGWB hinge on its power-law energy spectrum density in relation to the PLIS curve. If the spectrum surpasses the PLIS curve, detection for the SGWB is anticipated; however, if it falls below the curve, detection feasibility may be limited by the existing detector configuration.

In addition to following a power-law form, the SGWB can also adhere to other forms, such as the first-order

PT, where the energy spectral density

$$\Omega_{\text{gw}}(f) = \tilde{\Omega}(\theta)\mathcal{S}(f, \tilde{f}). \quad (22)$$

Here, $\tilde{\Omega}(\theta)$ signifies the peak energy spectral density at the peak frequency \tilde{f} , with the spectral function $\mathcal{S}(f, \tilde{f})$ being contingent upon the cosmological model. To address this disparity, Schmitz et.al introduced the PIS curve [31]:

$$\Omega_{\text{PIS}}(\tilde{f}) = \left[\frac{2T_{\text{tot}}}{1 + \delta_{\text{AB}}} \int_{f_{\text{min}}}^{f_{\text{max}}} df \frac{\bar{\Gamma}_{IJ}^2(f)\mathcal{S}^2(f, \tilde{f})}{\hat{D}_{\text{AB}}(f)} \right]^{-1/2}. \quad (23)$$

Returning to Eq. (15), the SNR can be determined by

$$\rho = \frac{\tilde{\Omega}(\theta)}{\Omega_{\text{PIS}}(\tilde{f})}. \quad (24)$$

By selecting a particular set of parameters θ , the peak frequency \tilde{f} and peak energy spectrum density $\tilde{\Omega}(\theta)$ are specified. If the peak amplitude exceeds ρ_{thr} times the PIS curve, the detection of cosmological PT can be confirmed.

IV. BEYOND WEAK-SIGNAL LIMIT

The weak-signal limit is applicable in most scenarios, especially for the derivation of the sensitivity curves. However, in certain cases, the intensity of a SGWB could become comparable to or even higher than the detector noise. For instance, the foreground originating from Galactic double white dwarf (GDWD) can exceed the noise level of space-borne detector noise [61], and the foreground from BBHs can dominate over the noise of next-generation ground-based detectors [62]. In such cases, adopting the SNR beyond the weak-signal limit becomes necessary.

Assuming that all other conditions specified in Eq. (13) hold true, except for the weak-signal limit. Then for all channel pairs $\{IJ\}$ (or equivalently, $\{MN\}$), the expectation and variance of the detection measurement

$$\begin{aligned} \mu &= \langle \sum_{IJ} S_{IJ} \rangle \\ &= \sum_{IJ} \int_0^{T_{\text{tot}}} dt_0 \int_{-\infty}^{\infty} df \int_{-\infty}^{\infty} df' \langle \tilde{h}_I(f, t_0) \tilde{h}_J^*(f', t_0) \rangle \tilde{Q}_{IJ}(f', t_0) e^{-i2\pi(f-f')t_0} \\ &= \sum_{IJ} \int_0^{T_{\text{tot}}} dt_0 \int_0^{\infty} df \int_0^{\infty} df' \delta(f-f') \Gamma_{IJ}(f, t_0) S_h(f) \tilde{Q}_{IJ}(f', t_0) e^{-i2\pi(f-f')t_0} \\ &= \sum_{IJ} \frac{3H_0^2}{2\pi^2} \int_0^{T_{\text{tot}}} dt_0 \int_0^{\infty} df f^{-3} \Gamma_{IJ}(f, t_0) \Omega_{\text{gw}}(f) \tilde{Q}_{IJ}(f, t_0), \end{aligned} \quad (25)$$

$$\begin{aligned}
\sigma^2 &= \langle \mu^2 \rangle - \langle \mu \rangle^2 \\
&= \sum_{IJ,MN} \int_0^{T_{\text{tot}}} dt_0 \int_0^{T_{\text{tot}}} d\eta_0 \int_{-\infty}^{\infty} df \int_{-\infty}^{\infty} df' \int_{-\infty}^{\infty} d\omega \int_{-\infty}^{\infty} d\omega' \\
&\quad \times \left[\langle (\tilde{s}_I(f, t_0) \tilde{s}_J^*(f', t_0) - \langle \tilde{n}_I(f, t_0) \tilde{n}_J^*(f', t_0) \rangle) (\tilde{s}_M(\omega, \eta_0) \tilde{s}_N^*(\omega', \eta_0) - \langle \tilde{n}_M(\omega, \eta_0) \tilde{n}_N^*(\omega', \eta_0) \rangle) \rangle \right. \\
&\quad \left. - \langle \tilde{h}_I(f, t_0) \tilde{h}_J^*(f', t_0) \rangle \langle \tilde{h}_M(\omega, \eta_0) \tilde{h}_N^*(\omega', \eta_0) \rangle \right] \tilde{Q}_{IJ}(f', t_0) \tilde{Q}_{MN}^*(\omega', \eta_0) e^{-i2\pi(f-f')t_0} e^{-i2\pi(\omega-\omega')\eta_0} \\
&= 2 \sum_{IJ,MN} \int_0^{T_{\text{tot}}} dt_0 \int_0^{\infty} df \left[\langle \tilde{s}_I(f, t_0) \tilde{s}_M(f, t_0) \rangle \langle \tilde{s}_J(f, t_0) \tilde{s}_N(f, t_0) \rangle + \langle \tilde{s}_I(f, t_0) \tilde{s}_N(f, t_0) \rangle \langle \tilde{s}_J(f, t_0) \tilde{s}_M(f, t_0) \rangle \right] \\
&\quad \times \tilde{Q}_{IJ}(f, t_0) \tilde{Q}_{MN}^*(f, t_0) \\
&\approx \frac{1 + \delta_{AB}}{2} \left[\frac{3H_0^2}{2\pi^2} \right]^2 \sum_{IJ} \int_0^{T_{\text{tot}}} dt_0 \int_0^{\infty} df f^{-6} D_{AB}(f) |\tilde{Q}_{IJ}(f, t_0)|^2, \tag{26}
\end{aligned}$$

where the filter function \tilde{Q}_{IJ} is arbitrary. Furthermore, for the last line of Eq. (26) to be valid, it is necessary that the ORF for cross-correlation is significantly lower than that for auto-correlation, leading to

$$D_{AB}(f) = \mathcal{R}_A(f) \mathcal{R}_B(f) [\Omega_{n_A}(f) + \Omega_{\text{gw}}(f)] [\Omega_{n_B}(f) + \Omega_{\text{gw}}(f)]. \tag{27}$$

Combined with Eq. (25) and Eq. (26), the square of SNR can be obtained by

$$\rho^2 = \frac{\mu^2}{\sigma^2} = \frac{2}{1 + \delta_{AB}} \frac{[\sum_{IJ} \int_0^{T_{\text{tot}}} dt_0 \int_0^{\infty} df f^{-3} \Gamma_{IJ}(f, t_0) \Omega_{\text{gw}}(f) \tilde{Q}_{IJ}(f, t_0)]^2}{\sum_{IJ} \int_0^{T_{\text{tot}}} dt_0 \int_0^{\infty} df f^{-6} D_{AB}(f) |\tilde{Q}_{IJ}(f, t_0)|^2}. \tag{28}$$

From Eq. (28), it is evident that the extension from Eq. (12) to Eq. (13) guarantees an SNR of 0 in the absence of an SGWB signal.

According to the definition of a positive-definite inner product, which is applicable to any pair of complex functions A and B [26]:

$$(A, B) := \sum_{IJ} \int_0^{T_{\text{tot}}} dt_0 \int_0^{\infty} df A_{IJ}(f, t_0) B_{IJ}^*(f, t_0) D_{AB}(f), \tag{29}$$

Eq. (28) transitions to

$$\rho_{\text{opt}}^2 = \frac{2}{1 + \delta_{AB}} \frac{(\tilde{Q}_{IJ}(f, t_0), \frac{f^3 \Gamma_{IJ}^*(f, t_0) \Omega_{\text{gw}}(f)}{D_{AB}(f)})^2}{(\tilde{Q}_{IJ}(f, t_0), \tilde{Q}_{IJ}(f, t_0))}. \tag{30}$$

Maximizing the SNR yields the solution

$$\tilde{Q}_{IJ}(f, t_0) = \lambda \frac{f^3 \Gamma_{IJ}^*(f, t_0) \Omega_{\text{gw}}(f)}{D_{AB}(f)}, \tag{31}$$

with a real constant λ . Following the preceding derivation, the total SNR should be modified by

$$\rho_{\text{tot}} = \sqrt{\frac{2 T_{\text{tot}}}{1 + \delta_{AB}} \int_{f_{\text{min}}}^{f_{\text{max}}} df \frac{\bar{\Gamma}_{\text{tot}}^2(f) \Omega_{\text{gw}}^2(f)}{D_{AB}(f)}}. \tag{32}$$

In contrast to Eq. (15), Eq. (32) suggests that the SGWB detection can suffer negative impacts from the SGWB itself, especially in cases of loud SGWB. To visualize this

impact, plotting sensitivity curves is beneficial. Although a direct derivation of Ω_0 and Ω_{PLIS} directly from Eq. (19) and Eq. (23) based on Eq. (32) to generate the sensitivity curves proves challenging, these values can still be determined by inverting the SNR formula¹. Fig. 3 and Fig. 4 illustrate the PLIS and PIS curves correspondingly, with solid lines in red, green, and blue denoting TianQin, the TianQin I+II network, and the TianQin + LISA network², surpassing the weak-signal limit. Dashed lines including the weak-signal limit are provided for comparison. As an illustrative example, the spectral function for the PIS curves is determined by

$$S(f, \tilde{f}_i) = \frac{3.9(f/\tilde{f}_i)^{2.9}}{1 + 2.9(f/\tilde{f}_i)^{3.8}}. \tag{33}$$

Furthermore, the operation time is set at 1 year, resulting in a correlation time T_{tot} equal to half a year, four months, and half a year for TianQin, the TianQin I+II network, and the TianQin + LISA network, respectively.

While sensitivity curves exhibit minimal gaps with and without the weak-signal limit when the SNR remains below 10, a notable gap emerges as the SNR reaches 100,

¹ In this work, we utilize the Newton-Raphson method.

² Note that for the TianQin detector, the auto-correlations within the same channel are considered. In the case of detector networks, the cross-correlations between channels from different detectors are taken into consideration.

especially pronounced for the TianQin + LISA network, with gaps reaching up to an order of magnitude. This suggests that the energy spectral density predicted by the weak-signal limit needs to be raised by approximately an order of magnitude for detectability.

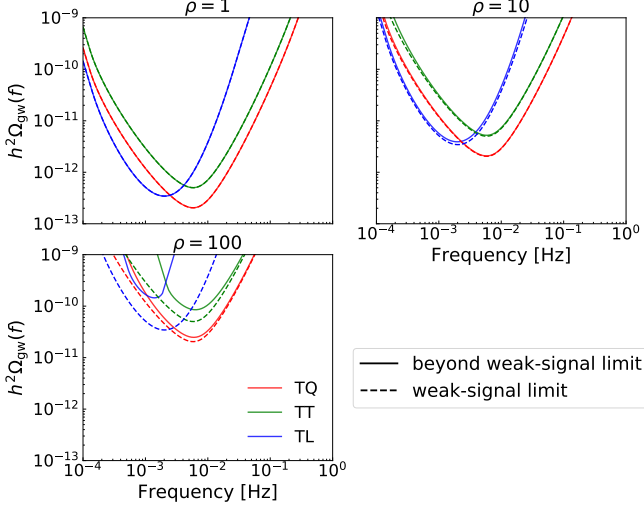


FIG. 3. PLIS curve with and without weak-signal limit.

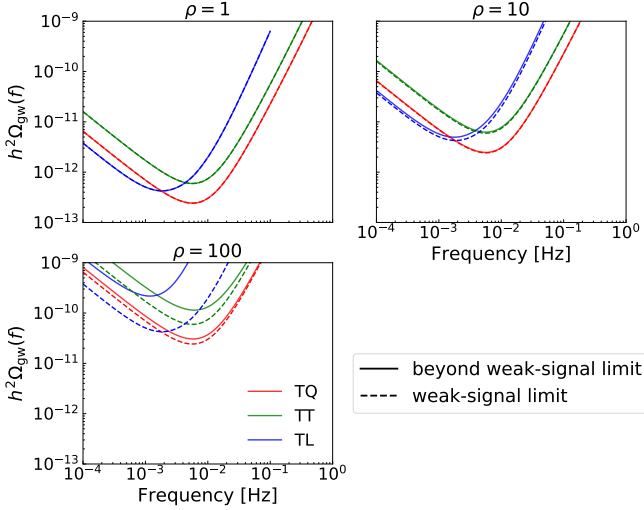


FIG. 4. PIS curve with and without weak-signal limit.

V. CASE STUDY

In this section, we will briefly discuss the potential sources that could generate loud SGWB in the mHz range, including DWDs and first-order PTs.

GDWDs are anticipated to produce foreground comparable to the noise of space-borne detectors. In terms of our previous work, the PSD of Galactic foreground can

TABLE I. Coefficients for the polynomial fit for the Galactic foreground. Each successive row corresponds to an increasing operation time T .

| T | a_0 | a_1 | a_2 | a_3 | a_4 | a_5 | a_6 |
|--------|-------|-------|--------|--------|---------|-------|-------|
| 0.5 yr | -18.7 | -1.23 | -0.801 | 0.832 | -1.96 | 3.09 | -2.38 |
| 1 yr | -18.7 | -1.34 | -0.513 | 0.0152 | -1.53 | 4.79 | -5.01 |
| 2 yr | -18.7 | -1.39 | -0.610 | 0.577 | 0.00242 | 0.578 | -4.39 |
| 4 yr | -18.7 | -1.30 | -0.872 | 0.266 | -5.12 | 15.6 | -15.5 |
| 5 yr | -18.7 | -1.32 | -0.322 | -1.68 | -4.49 | 21.6 | -22.6 |

be fit for through the following polynomial [37, 59]:

$$S_h(f) = \frac{20}{3} \left[10^{\sum_i a_i x^i} \right]^2, \quad (34)$$

where $x = \log(f/10^{-3} \text{ Hz})$, a_i represents the polynomial coefficients that are updated based on different operation times. The specific values of these coefficients can be found in Table I. In terms of Eq. (6), the energy spectrum density of Galactic foreground can be further derived.

Furthermore, it has been highlighted that the SGWB originating from extragalactic double white dwarfs (EDWDs) may exhibit significant intensity levels, leading to high SNR [59]. Without loss of generality, the corresponding energy spectrum density of SGWB can be described as the cumulative contribution from each binary system [28, 53, 64, 65]:

$$\Omega_{\text{gw}}(f) = \frac{f}{\rho_c} \int d\theta \int_0^{z_{\text{max}}} dz \frac{R_m(z) \frac{dE_{\text{gw}}}{df_s}(f_s, \theta)}{(1+z)H(z)}, \quad (35)$$

where the population parameter θ primarily encompasses the component masses of the system. Given the rarity of astrophysical compact stars at high redshifts due to the lack of star formation, the Hubble parameter $H(z)$ can be accurately approximated as $H_0 \sqrt{\Omega_m(1+z)^3 + \Omega_\Lambda}$ [66]. In this paper, we focus on the DA and DB white dwarfs, for which the mass distribution can be modeled by a Gaussian distribution with mean $\mu = 0.663 M_\odot$ and standard deviation $\sigma = 0.177 M_\odot$ [67]. The merger rate is directly linked to the redshift and can be expressed as follows [68]:

$$R_m(z) = R_0(1+z)^\kappa, \quad (36)$$

with the local merger rate R_0 and index κ . As suggested in Ref. [67], the R_0 is assumed to be within the range of 20 to 500 $\text{Mpc}^{-3} \text{ Myr}^{-1}$. The energy spectrum emitted in the source frame, denoted by dE_{gw}/df_s , is characterized by the frequency in the source frame $f_s = f(1+z)$ [69]. Given that the radius of a white dwarf significantly exceeds its Schwarzschild radius, it is reasonable to assume

TABLE II. Ingredients contributing to the SGWB spectra arising from first-order PTs. The parameter α_∞ determines the threshold for the weakest transition at which a portion of the vacuum energy converts into kinetic energy, driving the expansion of bubbles [63]. The sound speed is given by $c_s = 1/\sqrt{3}$, the redshifted, present-day value of the Hubble frequency $h_* = 1.65 \times 10^{-5} \left(\frac{T_*}{100 \text{ GeV}}\right) \left(\frac{g_*}{100 \text{ GeV}}\right)^{1/6} \text{ Hz}$.

| i | p | q | $\tilde{\Delta}_{i*}(v_w)$ | $\frac{\tilde{f}_{i*}}{\beta}$ | $\mathcal{S}_i(f, \tilde{f}_i)$ | $K_i(\alpha)$ |
|------|-----|---------------|-----------------------------------|-------------------------------------|--|---|
| col | 2 | 2 | $\frac{0.44v_w^3}{1+8.28v_w^3}$ | $\frac{0.31}{1-0.051v_w+0.88v_w^2}$ | $\left(\frac{f}{\tilde{f}_i}\right)^{2.8} \frac{3.8}{1+2.8(f/\tilde{f}_i)^{3.8}}$ | $\max[1 - \frac{\alpha_\infty}{\alpha}, 0]$ |
| sw | 1 | 2 | $0.157v_w H_* \tau_{\text{sw}}$ | $1.16(1 - c_s/v_w)$ | $\left(\frac{f}{\tilde{f}_i}\right)^3 \left[\frac{7}{4+3(f/\tilde{f}_i)^2}\right]^{7/2}$ | $\begin{cases} \kappa(\alpha_N) _{\alpha_N=\alpha}, \alpha \leq \alpha_\infty \\ \frac{\alpha_\infty}{\alpha} \kappa(\alpha_N) _{\alpha_N=\alpha_\infty}, \alpha > \alpha_\infty \end{cases}$ |
| turb | 1 | $\frac{3}{2}$ | $20v_w(1 - H_* \tau_{\text{sw}})$ | $1.33(1 - c_s/v_w)$ | $\left(\frac{f}{\tilde{f}_i}\right)^3 \frac{[1+(f/\tilde{f}_i)]^{3/11}}{1+8\pi f/h_*}$ | |

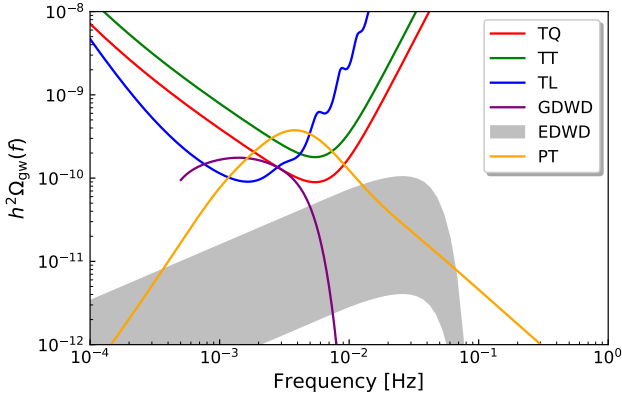


FIG. 5. Noise energy spectrum density of TianQin, the TianQin I+II network, the TianQin + LISA network, along with SGWB energy spectrum density of DWDs and first-order PTs.

that below the cut-off frequency where both stars come into contact, the binary systems consistently remain in the inspiral phase.

Regarding the first-order PTs³, we adopt the model mentioned in our previous study [59], where the energy spectrum density is formulated as

$$\Omega_{\text{gw}}(f) = \sum_i \tilde{\Omega}_i(\theta) \mathcal{S}_i(f, \tilde{f}_i). \quad (37)$$

Here, the sum accounts for the collision occurring during the PT, as well as the subsequent acoustic and turbulent phases. The redshifted peak frequency today for each source is given by [70]

$$\tilde{f}_i = \frac{\tilde{f}_{i*}}{\beta} \left(\frac{\beta}{H_*}\right) h_*, \quad (38)$$

³ Unless otherwise specified, we adopt the natural unit for discussions involving first-order PTs.

TABLE III. Detection SNR for Galactic foreground.

| | TQ | TT | TL |
|---------------|-----|-----|-----|
| With limit | 300 | 120 | 430 |
| Without limit | 170 | 69 | 96 |

where the peak frequency before redshifting, denoted as \tilde{f}_{i*} , depends on the sound speed c_s and the bubble velocity v_w . The parameter β/H_* represents PT duration normalized to the Hubble parameter, while h_* indicates the Hubble frequency. Additional details are provided in Table II.

When GWs are generated with the Hubble rate H_* , temperature T_* , and the total number of relativistic degrees of freedom g_* , the individual contributions factorizing in the redshift can be succinctly expressed as

$$\tilde{\Omega}_i(\theta) = 1.67 \times 10^{-5} \left(\frac{100}{g_*(T_*)}\right)^{1/3} \left(\frac{H_*}{\beta}\right)^p \times \left(K_i(\alpha) \frac{\alpha}{1+\alpha}\right)^q \tilde{\Delta}_{i*}(v_w), \quad (39)$$

where the indices p, q , the spectral function $\mathcal{S}_i(f, \tilde{f}_i)$, the efficiency factor K_i , and the peak amplitude $\tilde{\Delta}_{i*}$ are detailed in Table II. It is worth noting that the peak amplitude involves the timescale for acoustic production [63, 71, 72]

$$\tau_{\text{sw}} = \min[H_*^{-1}, R_*/U_f], \quad (40)$$

with the mean bubble separation R_* and the average square root of the fluid velocity U_f [73].

Figure 5 illustrates the SGWBs from various sources: the purple line represents the Galactic foreground with a one-year operation time, the gray region corresponds to the extragalactic background associated with the local merger rate ranging from 20 to 500 $\text{Mpc}^{-3} \text{ Myr}^{-1}$,

and the orange line signifies the cosmological background determined by the parameters $\{\alpha, \alpha_\infty, v_w, \beta/H_*, T_*\} = \{2, 1, 0.95, 50, 10^3 \text{ GeV}\}$. To facilitate comparison between the SGWB intensity and noise levels, the noise energy spectrum density of TianQin, the TianQin I+II network, and the TianQin + LISA network are shown in red, green, and blue lines, respectively. While the extragalactic background can near the detector noise level, both the Galactic foreground and cosmological background can exceed the noise. Taking the Galactic foreground as an example, Table. III presents the detection SNR within different detector configurations. It also provides the SNR under weak-signal conditions for the sake of comparison. In the weak-signal limit, the TianQin + LISA network achieves the highest SNR for detecting the Galactic foreground. As moving beyond the weak-signal limit, the SNR drops to approximately 20% for the TianQin + LISA network, whereas it remains around 60% for TianQin and the TianQin I+II network. Thus, TianQin demonstrates superior performance in terms of SNR.

The other two backgrounds exhibit considerable uncertainties in their parameters compared to the Galactic foreground. We will proceed to utilize SNR contour plots to determine the detectable parameter regions for them.

In Fig. 6, we present SNR contour plots for the extragalactic background, showcasing scenarios with and without the weak-signal limit in the left and right panels for comparison. Not surprisingly, an SNR threshold of 100 leads to significant variations in the detectable parameter regions between the two scenarios, especially for the TianQin + LISA network. Failure to achieve an SNR above 100 within one year of operation would shift the lower limit for κ from around 0 to 2.5, indicating a transition from a scenario with the weak-signal limit to one without it. This shift suggests that the adverse effects of loud SGWB self-generation on detection reduce the region of detectable parameters to a lesser extent than initially anticipated. On the other hand, assuming a constant merger rate with redshift ($\kappa = 0$), achieving an SNR exceeding 100 after 1 year of operation, under the weak-signal limit, would estimate the merger rate for EDWDs to be around $500 \text{ Mpc}^{-3} \text{ Myr}^{-1}$. However, this value falls considerably short of meeting the actual detection requirements.

A similar diminishing effect of parametric limitations can be observed in Fig. 7, where we follow Refs. [32, 34] and set the parameters $\{\alpha, \alpha_\infty, v_w\} = \{2, 1, 0.95\}$ for the first-order PTs. By setting α greater than α_∞ , the SGWB is anticipated to involve the collision, acoustic, and turbulent phases; the bubble velocity v_w exceeding the sound speed c_s corresponds to detonation bubble collisions [74]. Note that, changing other PT parameters and the parameter degeneracy may also influence the results depicted in the Fig. 7. If the SNR surpasses 100 after 1 year of operation, the temperature T_* is expected to be significantly greater than 10 GeV, while the PT duration β/H_* should be less than 10^2 . The detectable region for these two parameters can expand notably by

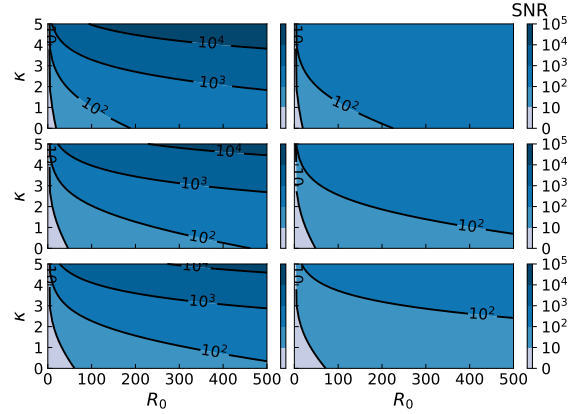


FIG. 6. SNR contour plots for the SGWB resulting from extragalactic DWD. The left-hand and right hand panels refer to the scenarios with and without weak-signal limit, considering a one-year operation time.

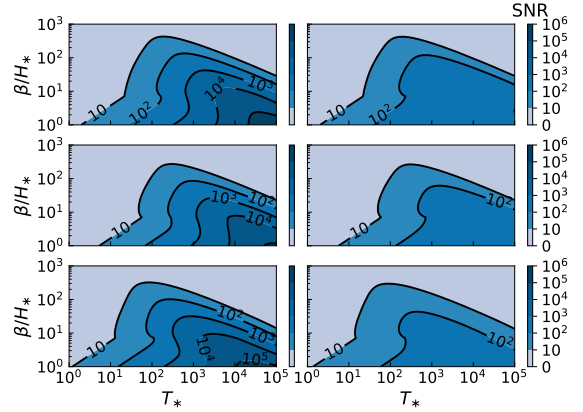


FIG. 7. SNR contour plots for the SGWB resulting from first-order PTs. The left-hand and right hand panels refer to the scenarios with and without weak-signal limit, considering a one-year operation time.

utilizing the weak-signal limit, leading to potential misjudgments in detection. It is important to highlight that, due to the wide range of variability in fixed parameters, effectively constraining the parameters of PTs remains a challenging task.

VI. CONCLUSIONS AND DISCUSSIONS

In this paper, we have derived the SNR tailored for detecting loud SGWB. By utilizing the improved SNR estimation, we have plotted PLIS and PIS curves for TianQin, the TianQin I+II network, and TianQin + LISA network to assess the detectable SGWB energy spectrum density over an operational period of 1 year. Our findings indicated that for SNR values below 10, the impact of considering or neglecting the weak-signal limit on the

results is minimal. However, when the SNR exceeds 100, applying the weak-signal limit can lead to a considerable overestimation of the detectable energy spectrum density. This overestimation becomes markedly pronounced for the TianQin + LISA network, where it may be inflated by approximately an order of magnitude.

Additionally, we have employed SNR contour plots to determine the detectable parameter regions for loud SGWBs generated by EDWDs and first-order PTs. With a chosen SNR threshold of 100, the prospect for detecting the SGWB from EDWDs, specifically DA and DB types, appears promising. This detection is grounded in a consistent merger rate exceeding $200 \text{ Mpc}^{-3} \text{ Myr}^{-1}$ surpassing varying redshifts, with the operation period extending over 1 year. On the other hand, while it is feasible to narrow down the parameters for first-order PTs by holding certain variables fixed, uncertainties in the underlying models permit only a broad constriction of the detectable parameter region.

We emphasize that our analysis can extend to the statistical inference of SGWB detection, which encompasses classical (frequentist) inference and Bayesian inference. The pivotal aspect lies in constructing the likelihood function. By estimating the expectation and variance in terms of Eq. (25) and Eq. (26), one can ensure that the likelihood function aligns more closely with the actual detection process, thereby minimizing bias in parameter estimation. This approach is not limited to space-borne detection [75–77], but is also relevant for next-generation ground-based detection [78, 79].

In this work, we assume the ideal case where the only

GW signal is SGWB. In reality, different signals will overlap and make the analysis more complicated. Fortunately, even if the SGWB is strong, it will not complicate the analysis of other sources. Taking the foreground from Galactic compact binaries as an example, it is expected that this foreground is comparable to or even stronger than instrument noise. However, when analyzing signals like the merger of massive black holes, the foreground can just be regarded as part of the PSD. That being said, the strong SGWB will inevitably raise the noise level, causing a decrease in the sensitivity.

ACKNOWLEDGMENTS

This work has been supported by the Guangdong Major Project of Basic and Applied Basic Research (Grant No. 2019B030302001), the National Key Research and Development Program of China (No. 2020YFC2201400), the Natural Science Foundation of China (Grants No. 12173104), the Natural Science Foundation of Guangdong Province of China (Grant No. 2022A1515011862), and the Guangdong Basic and Applied Basic Research Foundation (Grant No. 2023A1515030116). Z.C.L. is supported by the China Postdoctoral Science Foundation (Grant No. 2023M744094), and the Guangdong Basic and Applied Basic Research Foundation (Grant No. 2023A151511184). We also thank Fapeng Huang, Yun Jiang, and Jianwei Mei for helpful discussions.

-
- [1] N. Christensen, *Rept. Prog. Phys.* **82**, 016903 (2019), [arXiv:1811.08797 \[gr-qc\]](#).
 - [2] J. D. Romano (2019) [arXiv:1909.00269 \[gr-qc\]](#).
 - [3] J. C. N. de Araujo, O. D. Miranda, and O. D. Aguiar, *Phys. Rev. D* **61**, 124015 (2000), [arXiv:astro-ph/0004395](#).
 - [4] K. Martinovic, P. M. Meyers, M. Sakellariadou, and N. Christensen, *Phys. Rev. D* **103**, 043023 (2021), [arXiv:2011.05697 \[gr-qc\]](#).
 - [5] G. Agazie *et al.* (NANOGrav), *Astrophys. J. Lett.* **951**, L8 (2023), [arXiv:2306.16213 \[astro-ph.HE\]](#).
 - [6] H. Xu *et al.*, *Res. Astron. Astrophys.* **23**, 075024 (2023), [arXiv:2306.16216 \[astro-ph.HE\]](#).
 - [7] J. Antoniadis *et al.* (EPTA, InPTA:), *Astron. Astrophys.* **678**, A50 (2023), [arXiv:2306.16214 \[astro-ph.HE\]](#).
 - [8] D. J. Reardon *et al.*, *Astrophys. J. Lett.* **951**, L6 (2023), [arXiv:2306.16215 \[astro-ph.HE\]](#).
 - [9] R. Abbott *et al.* (KAGRA, Virgo, LIGO Scientific), *Phys. Rev. D* **104**, 022004 (2021), [arXiv:2101.12130 \[gr-qc\]](#).
 - [10] J. Luo *et al.* (TianQin), *Class. Quant. Grav.* **33**, 035010 (2016), [arXiv:1512.02076 \[astro-ph.IM\]](#).
 - [11] P. Amaro-Seoane *et al.* (LISA), (2017), [arXiv:1702.00786 \[astro-ph.IM\]](#).
 - [12] M. Tinto and J. W. Armstrong, *Phys. Rev. D* **59**, 102003 (1999).
 - [13] M. Tinto and S. V. Dhurandhar, *Living Rev. Rel.* **24**, 1 (2021).
 - [14] M. Vallisneri, J. Crowder, and M. Tinto, *Class. Quant. Grav.* **25**, 065005 (2008), [arXiv:0710.4369 \[gr-qc\]](#).
 - [15] C. J. Hogan and P. L. Bender, *Phys. Rev. D* **64**, 062002 (2001), [arXiv:astro-ph/0104266](#).
 - [16] M. Tinto, J. W. Armstrong, and F. B. Estabrook, *Phys. Rev. D* **63**, 021101 (2001).
 - [17] M. R. Adams and N. J. Cornish, *Phys. Rev. D* **89**, 022001 (2014), [arXiv:1307.4116 \[gr-qc\]](#).
 - [18] T. L. Smith and R. Caldwell, *Phys. Rev. D* **100**, 104055 (2019), [arXiv:1908.00546 \[astro-ph.CO\]](#).
 - [19] G. Boileau, N. Christensen, R. Meyer, and N. J. Cornish, *Phys. Rev. D* **103**, 103529 (2021), [arXiv:2011.05055 \[gr-qc\]](#).
 - [20] M. Muratore, D. Vetrugno, S. Vitale, and O. Hartwig, *Phys. Rev. D* **105**, 023009 (2022), [arXiv:2108.02738 \[gr-qc\]](#).
 - [21] J. Cheng, E.-K. Li, Y.-M. Hu, Z.-C. Liang, J.-d. Zhang, and J. Mei, *Phys. Rev. D* **106**, 124027 (2022), [arXiv:2208.11615 \[gr-qc\]](#).
 - [22] R. Hellings and G. Downs, *Astrophys. J. Lett.* **265**, L39 (1983).
 - [23] P. F. Michelson, *Monthly Notices of the Royal Astronomical Society* **227**, 933 (1987).
 - [24] N. Christensen, *Phys. Rev. D* **46**, 5250 (1992).
 - [25] E. E. Flanagan, *Phys. Rev. D* **48**, 2389 (1993), [arXiv:astro-ph/9305029 \[astro-ph\]](#).

- [26] B. Allen and J. D. Romano, *Phys. Rev.* **D59**, 102001 (1999), [arXiv:gr-qc/9710117 \[gr-qc\]](#).
- [27] C. Ungarelli and A. Vecchio, *Phys. Rev. D* **64**, 121501 (2001), [arXiv:astro-ph/0106538](#).
- [28] B. P. Abbott *et al.* (LIGO Scientific, Virgo), *Phys. Rev. Lett.* **120**, 091101 (2018), [arXiv:1710.05837 \[gr-qc\]](#).
- [29] Y. Hu, P.-P. Wang, Y.-J. Tan, and C.-G. Shao, *Astrophys. J.* **961**, 116 (2024).
- [30] E. Thrane and J. D. Romano, *Phys. Rev. D* **88**, 124032 (2013), [arXiv:1310.5300 \[astro-ph.IM\]](#).
- [31] K. Schmitz, *JHEP* **01**, 097 (2021), [arXiv:2002.04615 \[hep-ph\]](#).
- [32] C. Caprini *et al.*, *JCAP* **04**, 001 (2016), [arXiv:1512.06239 \[astro-ph.CO\]](#).
- [33] S. Kuroyanagi, T. Chiba, and T. Takahashi, *JCAP* **11**, 038 (2018), [arXiv:1807.00786 \[astro-ph.CO\]](#).
- [34] C. Caprini *et al.*, *JCAP* **03**, 024 (2020), [arXiv:1910.13125 \[astro-ph.CO\]](#).
- [35] P. Amaro-Seoane *et al.*, *Class. Quant. Grav.* **29**, 124016 (2012), [arXiv:1202.0839 \[gr-qc\]](#).
- [36] Z. Pan and H. Yang, *Class. Quant. Grav.* **37**, 195020 (2020), [arXiv:1910.09637 \[astro-ph.CO\]](#).
- [37] S.-J. Huang, Y.-M. Hu, V. Korol, P.-C. Li, Z.-C. Liang, Y. Lu, H.-T. Wang, S. Yu, and J. Mei, *Phys. Rev. D* **102**, 063021 (2020), [arXiv:2005.07889 \[astro-ph.HE\]](#).
- [38] A. Sharma and J. Harms, *Phys. Rev. D* **102**, 063009 (2020), [arXiv:2006.16116 \[gr-qc\]](#).
- [39] B. Zhou, L. Reali, E. Berti, M. Çalıřkan, C. Creque-Sarbinowski, M. Kamionkowski, and B. S. Sathyaprakash, *Phys. Rev. D* **108**, 064040 (2023), [arXiv:2209.01310 \[gr-qc\]](#).
- [40] J. Wu and J. Li, *Phys. Rev. D* **108**, 124047 (2023), [arXiv:2307.05568 \[gr-qc\]](#).
- [41] A. Torres-Orjuela, S.-J. Huang, Z.-C. Liang, S. Liu, H.-T. Wang, C.-Q. Ye, Y.-M. Hu, and J. Mei, (2023), [arXiv:2307.16628 \[gr-qc\]](#).
- [42] G. Mentasti, C. R. Contaldi, and M. Peloso, (2023), [arXiv:2312.10792 \[gr-qc\]](#).
- [43] H. Song, D. Liang, Z. Wang, and L. Shao, (2024), [arXiv:2401.00984 \[gr-qc\]](#).
- [44] N. J. Cornish, *Phys. Rev. D* **65**, 022004 (2002), [arXiv:gr-qc/0106058](#).
- [45] H. Kudoh, A. Taruya, T. Hiramatsu, and Y. Himemoto, *Phys. Rev. D* **73**, 064006 (2006), [arXiv:gr-qc/0511145](#).
- [46] G. Wang and W.-B. Han, *Phys. Rev. D* **104**, 104015 (2021), [arXiv:2108.11151 \[gr-qc\]](#).
- [47] D. Brzemiński, A. Hook, and G. Marques-Tavares, *JHEP* **11**, 061 (2022), [arXiv:2203.13842 \[hep-ph\]](#).
- [48] Z.-C. Liang, Z.-Y. Li, J. Cheng, E.-K. Li, J.-d. Zhang, and Y.-M. Hu, *Phys. Rev. D* **107**, 083033 (2023), [arXiv:2212.02852 \[astro-ph.GA\]](#).
- [49] B.-B. Ye, X. Zhang, M.-Y. Zhou, Y. Wang, H.-M. Yuan, D. Gu, Y. Ding, J. Zhang, J. Mei, and J. Luo, *Int. J. Mod. Phys. D* **28**, 09 (2019), [arXiv:2012.03260 \[gr-qc\]](#).
- [50] J. Mei *et al.* (TianQin), (2020), [10.1093/ptep/ptaa114](#), [arXiv:2008.10332 \[gr-qc\]](#).
- [51] S. Babak, A. Petiteau, and M. Hewitson, (2021), [arXiv:2108.01167 \[astro-ph.IM\]](#).
- [52] B. Allen, in *Les Houches School of Physics: Astrophysical Sources of Gravitational Radiation* (1996) pp. 373–417, [arXiv:gr-qc/9604033](#).
- [53] J. D. Romano and N. J. Cornish, *Living Rev. Rel.* **20**, 2 (2017), [arXiv:1608.06889 \[gr-qc\]](#).
- [54] N. J. Cornish and S. L. Larson, *Class. Quant. Grav.* **18**, 3473 (2001), [arXiv:gr-qc/0103075](#).
- [55] P. Welch, *IEEE Transactions on Audio and Electroacoustics* **15**, 70 (1967).
- [56] A. H. Nitz, T. Dal Canton, D. Davis, and S. Reyes, *Phys. Rev. D* **98**, 024050 (2018), [arXiv:1805.11174 \[gr-qc\]](#).
- [57] T. Dal Canton, A. H. Nitz, B. Gadre, G. S. Cabourn Davies, V. Villa-Ortega, T. Dent, I. Harry, and L. Xiao, *Astrophys. J.* **923**, 254 (2021), [arXiv:2008.07494 \[astro-ph.HE\]](#).
- [58] N. Seto, *Phys. Rev. D* **102**, 123547 (2020), [arXiv:2010.06877 \[gr-qc\]](#).
- [59] Z.-C. Liang, Y.-M. Hu, Y. Jiang, J. Cheng, J.-d. Zhang, and J. Mei, *Phys. Rev. D* **105**, 022001 (2022), [arXiv:2107.08643 \[astro-ph.CO\]](#).
- [60] Z.-C. Liang, Z.-Y. Li, E.-K. Li, J.-d. Zhang, and Y.-M. Hu, (2023), [arXiv:2307.01541 \[gr-qc\]](#).
- [61] G. Boileau, A. Lamberts, N. J. Cornish, and R. Meyer, *Mon. Not. Roy. Astron. Soc.* **508**, 803 (2021), [Erratum: *Mon. Not. Roy. Astron. Soc.* **508**, 5554–5555 (2021)], [arXiv:2105.04283 \[gr-qc\]](#).
- [62] T. Regimbau, M. Evans, N. Christensen, E. Katsavounidis, B. Sathyaprakash, and S. Vitale, *Phys. Rev. Lett.* **118**, 151105 (2017), [arXiv:1611.08943 \[astro-ph.CO\]](#).
- [63] J. Ellis, M. Lewicki, J. M. No, and V. Vaskonen, *JCAP* **06**, 024 (2019), [arXiv:1903.09642 \[hep-ph\]](#).
- [64] E. S. Phinney, (2001), [arXiv:astro-ph/0108028](#).
- [65] B. P. Abbott *et al.* (LIGO Scientific, Virgo), *Phys. Rev. Lett.* **116**, 131102 (2016), [arXiv:1602.03847 \[gr-qc\]](#).
- [66] N. Aghanim *et al.* (Planck), *Astron. Astrophys.* **641**, A6 (2020), [Erratum: *Astron. Astrophys.* **652**, C4 (2021)], [arXiv:1807.06209 \[astro-ph.CO\]](#).
- [67] P. A. Rosado, *Phys. Rev. D* **84**, 084004 (2011), [arXiv:1106.5795 \[gr-qc\]](#).
- [68] R. Abbott *et al.* (KAGRA, VIRGO, LIGO Scientific), *Phys. Rev. X* **13**, 011048 (2023), [arXiv:2111.03634 \[astro-ph.HE\]](#).
- [69] X.-J. Zhu, E. J. Howell, D. G. Blair, and Z.-H. Zhu, *Mon. Not. Roy. Astron. Soc.* **431**, 882 (2013), [arXiv:1209.0595 \[gr-qc\]](#).
- [70] R. Jinno and M. Takimoto, *Phys. Rev. D* **95**, 024009 (2017), [arXiv:1605.01403 \[astro-ph.CO\]](#).
- [71] M. Hindmarsh, S. J. Huber, K. Rummukainen, and D. J. Weir, *Phys. Rev. D* **96**, 103520 (2017), [Erratum: *Phys. Rev. D* **101**, 089902 (2020)], [arXiv:1704.05871 \[astro-ph.CO\]](#).
- [72] X. Wang, F. P. Huang, and X. Zhang, *JCAP* **05**, 045 (2020), [arXiv:2003.08892 \[hep-ph\]](#).
- [73] J. R. Espinosa, T. Konstandin, J. M. No, and G. Servant, *JCAP* **06**, 028 (2010), [arXiv:1004.4187 \[hep-ph\]](#).
- [74] M. Kamionkowski, A. Kosowsky, and M. S. Turner, *Phys. Rev. D* **49**, 2837 (1994), [arXiv:astro-ph/9310044](#).
- [75] C. Caprini, D. G. Figueroa, R. Flauger, G. Nardini, M. Peloso, M. Pieroni, A. Ricciardone, and G. Tasinato, *JCAP* **11**, 017 (2019), [arXiv:1906.09244 \[astro-ph.CO\]](#).
- [76] M. Pieroni and E. Barausse, *JCAP* **07**, 021 (2020), [Erratum: *JCAP* **09**, E01 (2020)], [arXiv:2004.01135 \[astro-ph.CO\]](#).
- [77] R. Flauger, N. Karnesis, G. Nardini, M. Pieroni, A. Ricciardone, and J. Torrado, *JCAP* **01**, 059 (2021), [arXiv:2009.11845 \[astro-ph.CO\]](#).
- [78] H. Zhong, R. Ormiston, and V. Mandic, *Phys. Rev. D* **107**, 064048 (2023), [Erratum: *Phys. Rev. D* **108**, 089902 (2023)], [arXiv:2209.11877 \[gr-qc\]](#).
- [79] D. S. Bellie, S. Banagiri, Z. Doctor, and V. Kalogera,

(2023), [arXiv:2310.02517 \[gr-qc\]](#).